






RESEARCH ARTICLE | AUGUST 30 2023

A sharp interface approach for wetting dynamics of coated droplets and soft particles

F. Pelusi ; F. Guglietta ; M. Sega ; O. Aouane ; J. Harting 



Physics of Fluids 35, 082126 (2023)

<https://doi.org/10.1063/5.0160096>



View
Online



Export
Citation

CrossMark

Articles You May Be Interested In

Impact dynamics of a viscous drop containing a particle

Physics of Fluids (August 2023)

Doubly ionized states of ethylene: Auger spectrum, potential energy surfaces and nuclear dynamics

J. Chem. Phys. (August 1989)

Evaluation of four-pole parameters for a straight pipe with a mean flow and a linear temperature gradient

J Acoust Soc Am (April 1981)

A sharp interface approach for wetting dynamics of coated droplets and soft particles

Cite as: Phys. Fluids **35**, 082126 (2023); doi: [10.1063/5.0160096](https://doi.org/10.1063/5.0160096)

Submitted: 30 May 2023 · Accepted: 9 August 2023 ·

Published Online: 30 August 2023



View Online



Export Citation



CrossMark

F. Pelusi,^{1,a)} F. Guglietta,^{1,b)} M. Segal,² O. Aouane,¹ and J. Harting^{1,3}

AFFILIATIONS

¹Helmholtz Institute Erlangen-Nürnberg for Renewable Energy (IEK-11), Forschungszentrum Jülich GmbH, Cauerstraße 1, 91058 Erlangen, Germany

²Department of Chemical Engineering, University College London, London WC1E 7JE, United Kingdom

³Department of Chemical and Biological Engineering and Department of Physics, Friedrich-Alexander-Universität Erlangen-Nürnberg, Cauerstraße 1, 91058 Erlangen, Germany

^{a)}Present address: Istituto per le Applicazioni del Calcolo (IAC), Consiglio Nazionale delle Ricerche (CNR), Via dei Taurini 19, 00185 Rome, Italy. Author to whom correspondence should be addressed: f.pelusi@iac.cnr.it

^{b)}Present address: Department of Physics and INFN, Tor Vergata University of Rome, Via della Ricerca Scientifica 1, 00133, Rome, Italy.

ABSTRACT

The wetting dynamics of liquid particles, from coated droplets to soft capsules, holds significant technological interest. Motivated by the need to simulate liquid metal droplets with an oxidized surface layer, in this work, we introduce a computational scheme that allows us to simulate droplet dynamics with general surface properties and model different levels of interface stiffness, also describing cases that are intermediate between pure droplets and capsules. Our approach is based on a combination of the immersed boundary and the lattice Boltzmann methods. Here, we validate our approach against the theoretical predictions in the context of shear flow and static wetting properties, and we show its effectiveness in accessing the wetting dynamics, exploring the ability of the scheme to address a broad phenomenology.

© 2023 Author(s). All article content, except where otherwise noted, is licensed under a Creative Commons Attribution (CC BY) license (<http://creativecommons.org/licenses/by/4.0/>). <https://doi.org/10.1063/5.0160096>

I. INTRODUCTION

The wetting of a solid surface by a liquid coincides with its ability to preserve contact with the liquid.^{1–4} The wettability of a solid substrate by a pure droplet is quantified by the droplet's equilibrium contact angle θ_{eq} , which, in turn, is determined by the balance between adhesive and cohesive forces of the three phases involved (solid, liquid, and vapor). At the macroscopic scale, Young's equation⁵ describes this balance as

$$\cos \theta_{eq} = \frac{\sigma_{sl} - \sigma_{sg}}{\sigma}, \quad (1)$$

where σ_{sl} , σ_{sg} , and σ are the solid–liquid, solid–gas, and liquid–gas surfaces, respectively. Equation (1) also estimates the degree of wettability, making the distinction between poor ($\theta_{eq} > 90^\circ$) and good ($\theta_{eq} < 90^\circ$) wetting regimes. Out of equilibrium, the additional complexities arising from time dependence and viscous dissipation make dynamic wetting critical to a wide range of phenomena, including

droplet spreading, capillary rise, imbibition, and more complex situations like fluid displacement in porous media or multiphase flow in oil recovery.^{6–9} The recent development of new catalytic devices, for example, requires the usage of liquid metals and metal alloys in the form of catalytic liquid droplets adsorbed on porous solid support.^{10,11} However, several liquid metals, such as gallium and gallium-based alloys, oxidize when exposed to air and an inherent oxide layer appears on top of the surface. This oxide layer acts as a solid-like “skin,” encapsulating a liquid metal core^{12,13} and changing the wetting properties of the droplet.^{14–17} Another example concerns the so-called liquid marbles, realized by rolling a small liquid droplet in poorly wetting powder. Because of the layer of powder grains at the liquid–air interface, the wetting of these droplets is inhibited,^{18,19} as required in some recent technological and microfluidic applications.^{20,21} The lattice Boltzmann (LB) method has been used for decades to address problems in wettability.^{22–33} A typical strategy used to simulate droplets within the framework of LB includes introducing nonideal interface

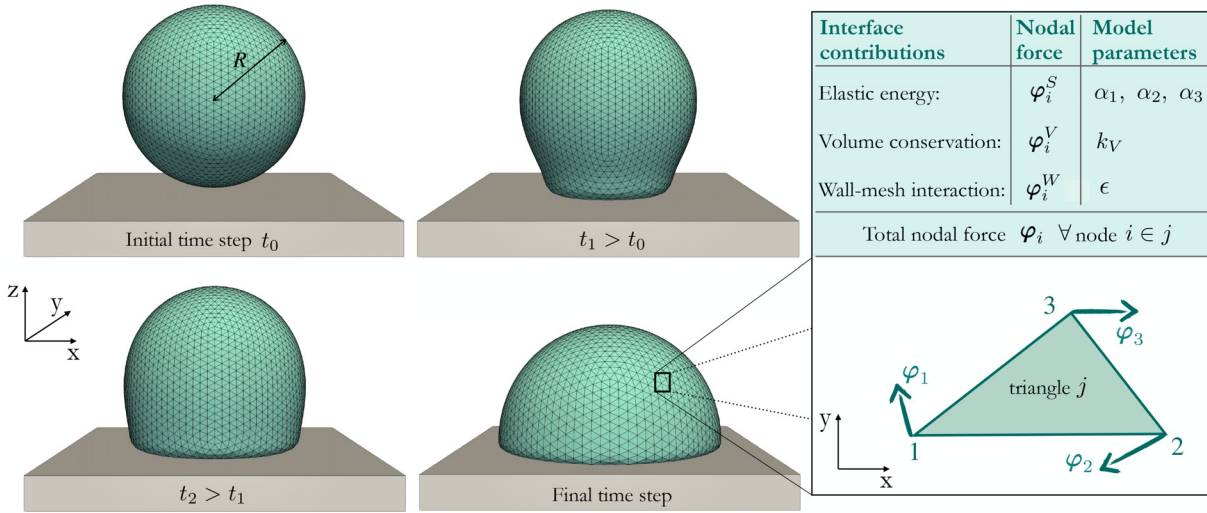


FIG. 1. Sketch of the wetting dynamics of a generic particle with initial radius R initially placed in contact with a flat wall. The interface is resolved with a 3D triangular mesh. On each triangular face j , some force contributions φ are computed and distributed to the vertices $i \in j$, with the aim to consider (i) the interface elasticity/rigidity, (ii) the volume conservation, and (iii) the wall–particle interaction. We also report the corresponding involved parameters.

force models such as the Shan–Chen³⁴ and the Free-Energy ones.³⁵ However, these approaches model a diffuse interface. Simulating droplets with complex rheology, specifically coated droplets, including liquid metal ones with an oxide layer or liquid marbles, requires the use of a constitutive law for the interface. In this case, it is more convenient to use a method that reproduces the sharp-interface limit of hydrodynamics. In addition, pseudopotential or free-energy approaches do not easily allow modelling a behavior that, as it is typical for coated droplets, is intermediate between the case of a pure droplet and that of a capsule, as is the case for coated droplets. For these reasons, here we have opted for combining the LB model with an immersed boundary (IB) method, which naturally preserves the hydrodynamic sharp-interface limit, to simulate the complex droplet’s wetting dynamics (see Fig. 1).

Our goal is to introduce a comprehensive numerical approach that allows modeling droplets with complex interfacial properties in a consistent way. Here, we model the interface as a 3D triangular mesh and employ a constitutive law based on the theory of Barthès-Biesel and Rallison³⁶ to explore the case of coated droplets. This approach allows us to describe in a continuous way the transition from pure droplets to capsule-like models by minimizing the number of involved parameters. We provide a validation of our IBLB numerical simulations against the theoretical prediction in the case of a simple shear flow experiment. Then, we perform wetting dynamics simulations, which show good agreement with experimental observations in the case of a pure droplet, and we explore the range of accessible contact angles in terms of the involved parameters and the intensity of the interaction with the wall. With this approach, we aim to provide a qualitative approximation of the mechanical behavior of droplets with a complete and wide range of interfacial properties. Nevertheless, the model can be further refined to include additional interface properties, enhancing its accuracy and applicability such as an extended model to mimic the oxidized layer thickness when dealing with liquid metal droplets.

This paper is organized as follows: in Sec. II, we describe the interface model introduced in the IBLB framework. Then, in Sec. III, we summarize the main features of the IBLB model employed. The benchmark of a droplet in a simple shear flow is shown in Sec. IV. In the context of the wetting dynamics, Sec. V A reports a model validation, while all wetting dynamics facets are analyzed and discussed in Sec. V B. Results are summarized in Sec. VI.

II. INTERFACE MODEL

In this section, we describe the theoretical model employed in this work to simulate a generic soft particle. Following Barthès-Biesel and Rallison,³⁶ we consider a two-dimensional, isotropic, and homogeneous elastic interface with no bending resistance. Its mechanical response is characterized by an interface strain energy $w_S = w_S(I_1, I_2, \alpha_1, \alpha_2, \alpha_3)$, which is written in terms of the principal strain invariants $I_{1,2}$ and three parameters $\alpha_{1,2,3}$ as³⁶

$$w_S(I_1, I_2, \alpha_1, \alpha_2, \alpha_3) = w_{S,0} + \frac{1}{2}(\alpha_1 - \alpha_3)\log(I_2 + 1) + \frac{1}{8}(\alpha_1 + \alpha_2)\log^2(I_2 + 1) + \alpha_3 \left[\frac{1}{2}(I_1 + 2) - 1 \right], \quad (2)$$

where $w_{S,0}$ is a reference value. I_1 and I_2 quantify the strain and dilation state of the membrane, respectively. The parameters $\alpha_{1,2,3}$, instead, characterize the material properties: the prestress α_1 is an isotropic tension without an applied load; α_2 is the resistance against area dilatation; and α_3 is the resistance against shear deformation (i.e., the strain modulus). For the sake of simplicity, hereafter we will refer to these three parameters as $\alpha = (\alpha_1, \alpha_2, \alpha_3)$. Concerning their choice, we distinguish the two main classes of prestressed ($\alpha_1 > 0$) and non-prestressed ($\alpha_1 = 0$) particles. For the latter class, an appropriate

TABLE I. List of system models that can be explored by tuning the parameters α_1 , α_2 , and α_3 in the interface model for a generic particle reported in Eq. (2). The left and right tables refer to the prestressed and non-pre-stressed particle classes, respectively. For each model, we display the corresponding fitting parameters a , b , c , and d appearing in Eq. (25).

Prestressed particles					
$\alpha = (\alpha_1, \alpha_2, \alpha_3)$	Model	a	b	c	d
$\alpha = \bar{\alpha}(1, 0, 0)$	Pure droplet	0.78	0.42	0.0	1.0
$\alpha = \bar{\alpha}(1, 0, 1)$	Softly coated droplet	0.87	0.5	0.0	1.0
$\alpha = \bar{\alpha}(1, 1, 1)$	Rigidly coated droplet	0.91	0.55	0.0	1.0
Non-pre-stressed particles					
$\alpha = (\alpha_1, \alpha_2, \alpha_3)$	Model	a	b	c	d
$\alpha = \bar{\alpha}(0, 0, 1)$	Pure elastic capsule	0.71	2.0	0.2	0.75
$\alpha = \bar{\alpha}(0, 1, 1)$	Non-pre-stressed capsule	0.7	1.6	0.2	0.75

combination of α_2 and α_3 leads to the well-known Skalak³⁷ and Neo-Hookean³⁸ models. By conveniently tuning these parameters, one can switch from a pure droplet ($\alpha = (\sigma, 0, 0)$, where σ is the surface tension) to a pure elastic capsule ($\alpha = (0, 0, \alpha_3 > 0)$) and describe intermediate and more complex situations. In particular, in this work, we also consider the classes of particles with $\alpha = (\alpha_1 > 0, 0, \alpha_3 > 0)$ and $\alpha = (\alpha_1 > 0, \alpha_2 > 0, \alpha_3 > 0)$. We call the first type of particle a “softly coated droplet” because it has the characteristic surface tension term of a droplet but also a strain modulus because of $\alpha_3 > 0$. Because of the presence of a dilatational term $\alpha_2 > 0$, we call the second type “rigidly coated droplet.” Here, we argue that the latter case could be used to describe the interfacial properties of particles like liquid metal droplets with oxidized surfaces. In Table I, we summarize the type of particles investigated in this work.

In order to check that Eq. (2) leads to the correct particle dynamics, we consider the case of a shear flow experiment, where a particle with initial radius R and dynamic viscosity μ is placed between two distant moving walls that generate a shear rate $\dot{\gamma}$ (see top panel of Fig. 2). In this setup, the time-dependent motion of the particle shape may be distinguished into two contributions: a solid body rotation and a stretching. Notice that the interface may rotate via a tank-treading motion despite the particle reaching its steady state. This means that at this stage, the interface deformation is constant in time at Eulerian point \mathbf{x} , but it is not constant by looking at point X on the interface. Thus, following concepts and notation of Ref. 36, the time-evolution of the dimensionless position \mathbf{x} (i.e., the position divided by the initial radius R), which is representative of the deformation field, reads

$$\mathbf{x} = \mathbf{X} + \beta[\mathbf{K} \cdot \mathbf{X} + \mathbf{X}\mathbf{X} \cdot (\mathbf{J} - \mathbf{K}) \cdot \mathbf{X}], \quad (3)$$

where $\beta \ll 1$ is the expansion coefficient around the initial spherical position (we truncate the equation at the leading order in β), while \mathbf{J} and \mathbf{K} are two symmetric and traceless second-rank tensors that depend only on time. It follows that the instantaneous external shape of the particle r can be computed in terms of the norm of Eq. (3), together with its normal \mathbf{n} ,³⁶

$$r \equiv |\mathbf{x}| = 1 + \beta \mathbf{X} \cdot \mathbf{J} \cdot \mathbf{X} = 1 + \beta \frac{\mathbf{x} \cdot \mathbf{J} \cdot \mathbf{x}}{r^2}, \quad (4a)$$

$$\mathbf{n} = \frac{\mathbf{x}}{r} + 2\beta \left[\frac{\mathbf{x}\mathbf{x} \cdot \mathbf{J} \cdot \mathbf{x}}{r^3} - \frac{\mathbf{J} \cdot \mathbf{x}}{r} \right]. \quad (4b)$$

Since in Eq. (4) only tensor \mathbf{J} appears, it means that \mathbf{J} describes the overall deformation (i.e., the stretching contribution), while \mathbf{K} describes the motion on the interface (i.e., the solid body rotation).³⁶ We remark that \mathbf{J} is traceless because of the volume conservation constraint, whereas this property for \mathbf{K} can be checked as *a posteriori*. In the limit of small deformations, the evolution equations for \mathbf{J} and \mathbf{K} are given by³⁶

$$\begin{cases} \frac{\mathfrak{D}}{\mathfrak{D}t} \mathbf{K} = \frac{5E}{2\lambda + 3} + \frac{\mathbf{L}}{2\lambda + 3} + \frac{M(6\lambda + 4)}{(2\lambda + 3)(19\lambda + 16)} \\ \frac{\mathfrak{D}}{\mathfrak{D}t} (\mathbf{J} - \mathbf{K}) = \frac{2}{19\lambda + 16} \mathbf{M}, \end{cases} \quad (5)$$

where

$$\frac{\mathfrak{D}\mathbf{A}}{\mathfrak{D}t} = \frac{d\mathbf{A}}{dt} - (\boldsymbol{\Omega} \cdot \mathbf{A} - \mathbf{A} \cdot \boldsymbol{\Omega}) \quad (6)$$

is the Jaumann derivative³⁶ applied to a generic tensor \mathbf{A} , which takes into account the rotation of the particle with the vorticity of the external fluid. \mathbf{E} and $\boldsymbol{\Omega}$ are the symmetric and asymmetric parts of the velocity gradient, respectively; λ is the viscosity ratio between inside and outside fluids, and

$$\mathbf{L} = 4(\alpha_2 + \alpha_3)\mathbf{J} - (6\alpha_2 + 10\alpha_3)\mathbf{K}, \quad (7a)$$

$$\mathbf{M} = -4(\alpha_1 + 2\alpha_2 + 2\alpha_3)\mathbf{J} + (12\alpha_2 + 16\alpha_3)\mathbf{K}. \quad (7b)$$

By numerically integrating Eq. (5), it is possible to obtain information on the transient deformation dynamics since the tensor \mathbf{J} is directly related to the particle deformation as³⁹

$$D = \text{Ca} (J_{11}^2 + J_{12}^2)^{1/2}, \quad (8)$$

where $\text{Ca} = \mu R \dot{\gamma} / \alpha$ is the capillary number. In the latter definition, one can consider $\alpha = \alpha_1 = \sigma$ for a pure droplet or $\alpha = \alpha_3$ for a pure capsule. For the sake of simplicity, we fix the values of parameters α_1 , α_2 , and α_3 to be equal to the same value $\bar{\alpha}$, and we will refer to this triad of values simply as $\alpha = \bar{\alpha}(0/1, 0/1, 0/1)$, with the vector elements turned on (1) and off (0) with the corresponding model (see Table I).

III. NUMERICAL IMPLEMENTATION

The dynamics of the inner and outer fluid is simulated using a single-component lattice Boltzmann (LB) method in terms of the fluid particle populations $f_i(\hat{\mathbf{x}}, t)$. The latter represents the probability distribution function of finding a fluid particle in a discrete lattice (Eulerian) node $\hat{\mathbf{x}}$ at a discrete time t . The corresponding macroscopic behavior is recovered in the long-wavelength limit, which allows the link with the Navier–Stokes equations. Indeed, the solutions of the Navier–Stokes equation for the total density and momentum are easily accessible from the populations as $\rho(\hat{\mathbf{x}}, t) = \sum_i f_i(\hat{\mathbf{x}}, t)$ and $\rho(\hat{\mathbf{x}}, t)\mathbf{u}(\hat{\mathbf{x}}, t) = \sum_i \mathbf{c}_i f_i(\hat{\mathbf{x}}, t)$, respectively, with \mathbf{c}_i representing a set of 19 discrete velocities ($i = 0, \dots, 18$) living on a three-dimensional lattice (i.e., we employ a D3Q19 LB model). The dynamics of f_i is ruled

by a continuous succession of propagation and collision steps, as highlighted by the discretized Boltzmann equation^{40,41}

$$\begin{aligned}
 & f_i(\hat{\mathbf{x}} + \mathbf{c}_i \Delta t, t + \Delta t) - f_i(\hat{\mathbf{x}}, t) \\
 &= -\frac{\Delta t}{\tau} \left[f_i(\hat{\mathbf{x}}, t) - f_i^{(eq)}(\hat{\mathbf{x}}, t) \right] \\
 &+ w_i \left(1 - \frac{\Delta t}{2\tau} \right) \left(\frac{(\mathbf{c}_i - \mathbf{u}) \cdot \mathbf{F}}{c_s^2} + \frac{(\mathbf{c}_i \cdot \mathbf{F})(\mathbf{c}_i \cdot \mathbf{u})}{c_s^4} \right) \Delta t, \quad (9)
 \end{aligned}$$

where Δt is the time step. The propagation of f_i on the lattice is described by the lhs of Eq. (9) with the help of \mathbf{c}_i , while the single-relaxation-time BGK approximation of the collision operator appears as the first term in the rhs. The latter has the aim of modeling the relaxation of f_i toward the equilibrium distribution $f_i^{(eq)}(\hat{\mathbf{x}}, t)$, represented as the local Maxwellian distribution

$$f_i^{(eq)}(\hat{\mathbf{x}}, t) = w_i \rho \left[1 + \frac{u_k c_{i,k}}{c_s^2} + \frac{u_k u_j (c_{i,k} c_{i,j} - c_s^2 \delta_{kj})}{2c_s^2} \right]. \quad (10)$$

The relaxation process lasts for a relaxation time τ . In Eq. (10), $f_i^{(eq)}$ is weighted by the lattice-dependent weights w_i and depends on the speed of sound $c_s = \Delta \hat{x} / (\sqrt{3} \Delta t)$, where $\Delta \hat{x}$ is the lattice spacing (the weight w_i in the employed D3Q19 model are $w_i = 1/3$ for $i = 0, w_i = 1/18$ for $i = 1 \dots 6, w_i = 1/36$ for $i = 7 \dots 18$). The last term of Eq. (9) refers to the forcing implementation following the Guo scheme,⁴² where \mathbf{F} is the force acting on the fluid. Notice that this forcing scheme modifies the fluid velocity as $\rho(\hat{\mathbf{x}}, t) \mathbf{u}(\hat{\mathbf{x}}, t) = \sum_i \mathbf{c}_i f_i(\hat{\mathbf{x}}, t) + \mathbf{F} \Delta t / 2$ to guarantee the second-order space–time accuracy. In our simulations, we keep fixed to unity, both $\Delta \hat{x}$ and Δt . Furthermore, the fluid dynamic viscosity μ in LB models is related to the relaxation time τ as $\mu = c_s^2 \rho (\tau - 1/2)$. Here, we keep the viscosity ratio λ fixed to unity since the investigation of the role played by λ goes beyond the purpose of this work.

Then, to simulate the interface of a coated droplet or soft particle immersed in the surrounding LB fluid, we model the spherical particle interface using a 3D triangular mesh generated from a recursive refining of an icosahedron. Thus, the mesh resolution is defined in terms of the total number of triangular faces N_f (see Fig. 6 for a pictorial view of particles with different resolutions). To couple the soft particle dynamics with that of the surrounding fluid, we use the immersed boundary (IB) method, i.e., a fluid–mesh interaction method developed for the first time by Peskin⁴³ and based on the distinction between interface (Lagrangian) nodes $\mathbf{q}(t)$ and fluid (Eulerian) nodes $\hat{\mathbf{x}}$. The resulting coupling is distinct in two operations, i.e., interpolation and spreading. The interpolation operation consists of the computation of the i -th interface-node velocity $\dot{\mathbf{q}}_i(t)$ from the fluid one ($\mathbf{u}(\hat{\mathbf{x}}, t)$) as (note that Eq. (11) causes the velocity of the surface to be equal to the fluid velocity, ensuring thus the no-slip boundary condition at the interface^{41,44})

$$\dot{\mathbf{q}}_i(t) = \sum_{\hat{\mathbf{x}}} \mathbf{u}(\hat{\mathbf{x}}, t) \delta_D(\hat{\mathbf{x}} - \mathbf{q}_i(t)) \Delta \hat{x}^3. \quad (11)$$

This operation allows updating the node position $\mathbf{q}_i(t)$ as

$$\mathbf{q}_i(t + \Delta t) = \mathbf{q}_i(t) + \dot{\mathbf{q}}_i(t) \Delta t. \quad (12)$$

Then, the spreading operation is an interpolation of the interface nodal force to the fluid one, which allows making the latter aware of the

presence of the interface: at this step, the total force (volume-) density the particle exerts on the fluid at the Eulerian node $\hat{\mathbf{x}}$ is given by

$$\mathbf{F}(\hat{\mathbf{x}}, t) = \sum_i \boldsymbol{\varphi}_i(t) \delta_D(\hat{\mathbf{x}} - \mathbf{q}_i(t)), \quad (13)$$

where $\boldsymbol{\varphi}_i$ is the total force on the Lagrangian node i , and the sum runs over all Lagrangian nodes. Both operations involve the so-called discrete delta function δ_D , which is used to approximate the Dirac delta function on our lattice and is defined as^{41,43,44}

$$\delta_D(\hat{\mathbf{x}}) = \frac{1}{\Delta \hat{x}^3} \phi_4(\hat{x}) \phi_4(\hat{y}) \phi_4(\hat{z}), \quad (14)$$

where $\phi_4(r)$ is the “interpolation stencil” involving four Eulerian nodes along each coordinate axis⁴⁵ and defined as follows:

$$\phi_4(\hat{x}) = \begin{cases} \frac{1}{8} \left(3 - 2|\hat{x}| + \sqrt{1 + 4|\hat{x}| - 4\hat{x}^2} \right) & 0 \leq |\hat{x}| \\ \frac{1}{8} \left(5 - 2|\hat{x}| - \sqrt{-7 + 12|\hat{x}| - 4\hat{x}^2} \right) & \Delta \hat{x} \leq |\hat{x}| \leq 2\Delta \hat{x} \\ 0 & 2\Delta \hat{x} \leq |\hat{x}|. \end{cases} \quad (15)$$

The resulting IBLB method has been largely used to simulate the dynamics of capsules^{45–49} and red blood cells.^{50–54} However, only a few works employed this method for simulating droplet dynamics.^{55–57} A detailed step-by-step description of the IBLB algorithm implementation can be found in Ref. 41.

In our implementation, the total nodal force $\boldsymbol{\varphi}_i$, appearing in Eq. (13) and acting on the i -th node at position \mathbf{r}_i at time t , is given by the sum of several contributions, i.e.,

$$\boldsymbol{\varphi}_i = \boldsymbol{\varphi}_i^S + \boldsymbol{\varphi}_i^V + \boldsymbol{\varphi}_i^W. \quad (16)$$

Each contribution plays a distinct role. First of all, $\boldsymbol{\varphi}_i^S$ incorporates the information on the elastic properties of the interface. Thus, we compute this nodal force term as

$$\boldsymbol{\varphi}_i^S = -\frac{\partial}{\partial \{\mathbf{q}_i\}} w_S(\{\mathbf{q}_i\}), \quad (17)$$

where w_S is the generalized strain energy defined in Eq. (2). Equation (17) is calculated using a first-order finite element method as described in Ref. 45. Then, because we are dealing with incompressible fluids, we need to consider a volume conservation constraint. With this aim, we follow Ref. 45 and we write the nodal volume force contribution $\boldsymbol{\varphi}_i^V$ as⁵⁸

$$\boldsymbol{\varphi}_i^V = -\frac{\partial}{\partial \{\mathbf{q}_i\}} w_V(\{\mathbf{q}_i\}), \quad (18)$$

where $w_V = k_V (V - V_0)^2 / 2V_0$ is the volume energy. In this definition of the volume energy, k_V refers to the volume-force coefficient, and it is kept fixed to 1. $V = \sum_j V_j$ is the instantaneous total particle volume, with the index j running over the number of faces N_f (note that V is functionally dependent on $\{\mathbf{r}_i\}$), while V_0 is the initial total particle volume. Further details on how to compute nodal force contributions in Eqs. (17) and (18) can be found in Ref. 58. The last contribution in Eq. (16) corresponds to the wall–particle interaction, the key element for wetting dynamics simulations. The IBLB approach used in

this work involves only one single fluid component, and it is not possible to control the wall–fluid surface tensions σ_{sl} and σ_{sg} by introducing two different interactions as, for example, Huang and co-workers did in the case of multicomponent pseudopotential LB models.²⁴ However, many implementations of fluid–wall interactions in the case of single-component LB models^{59–61} use a pseudopotential-like fluid–wall interaction, which does not control σ_{sl} and σ_{sg} separately, but only their overall effect. These models work well in describing the wetting dynamics of droplets despite this limitation. In this work, we follow the same approach, and we introduce a Lennard–Jones interaction on behalf of the wall–particle interaction

$$\phi_i^W = 48\epsilon \left[\left(\frac{\zeta}{d_i} \right)^{12} - \frac{1}{2} \left(\frac{\zeta}{d_i} \right)^6 \right] \frac{\mathbf{d}_i}{d_i^2}, \quad (19)$$

where \mathbf{d}_i is the shortest displacement vector between the centroid of the triangle to which node i belongs and the wall surface, and $d_i = |\mathbf{d}_i|$. It means that the force is computed once for each triangle, and then it is distributed on its vertices. The choice of employing a Lennard–Jones interaction potential results from the necessity to model adhesive and repulsive forces between the droplet or particle and the surface. It follows the large amount of works based on molecular dynamics simulations, which successfully studied the behavior of nanodroplets or ridges on chemically patterned substrates.^{62–66} Notice that in this work, we set $\zeta = 0.5\Delta\hat{x}$ to have an interface–wall interaction that decays to zero after one lattice spacing, thus respecting as much as possible the microscopic range and tuning the interaction by changing only ϵ . The nodal force contributions and the corresponding parameters are summarized in Fig. 1.

By summarizing, the IBLB algorithm implemented in this work matches the following steps:⁴¹

1. Compute the nodal force ϕ_i on each node i [Eq. (16)];
2. Spread the nodal force to obtain the force acting on the fluid $\mathbf{F}(\hat{\mathbf{x}}, t)$ via Eq. (13);
3. Perform the LB integration step: compute equilibrium distributions [Eq. (10)], then apply the collision and perform the propagation. At this stage, $\mathbf{F}(\hat{\mathbf{x}}, t)$ enters in r.h.s. of Eq. (9);
4. Compute the fluid velocity $\mathbf{u}(\hat{\mathbf{x}}, t)$ from LB populations;
5. Interpolate the fluid velocity to compute the Lagrangian node velocity [Eq. (11)];
6. Update the position of each node $\mathbf{q}(t)$ via Eq. (12);
7. Iterate from step 1.

All simulations have been performed in a periodic domain in the x - and y -directions, while two walls are placed along the (vertical) z -direction. A half-node bounce-back rule implements second-order no-slip boundary conditions at the walls.⁴¹ Dimensional quantities are shown in lattice Boltzmann units (lbu).

Note that although this method is not able to capture particle breakup and coalescence, it provides an easy way to model different systems by simply tuning the α_i parameters, as detailed in Sec. II. The introduction of the wall–particle interaction [Eq. (19)] induces an accumulation of interface nodes on the wall–particle contact area. Such an aggregation is more prominent for high values of ϵ that are required for observing small contact angles and is responsible for a numerical instability in that regime. The remeshing technique may help to mitigate this problem, but since we are interested in large contact angles, this accumulation does not affect the results presented in this paper.

IV. BENCHMARK: SHEAR FLOW DYNAMICS

To showcase the versatility of the interface model proposed in Sec. II, we perform a double analysis by measuring the deformation of coated droplets and soft particles undergoing a shear flow. Indeed, on the one hand, we benchmark our model with what is known in the literature for the case of a pure droplet, while, on the other hand, we explore the different scenarios associated with each particle case listed in Table I. In this setup, we run simulations for particles with an initial radius $R = 19$ lbu, placed in a channel with a distance between the two walls $H = 128$ lbu. The system has the same size along the other two directions, x and y . In order to vary the capillary number Ca , we systematically tune the values of $\bar{\alpha}$, keeping fixed the shear rate $\dot{\gamma}$ by the constraint of low Reynolds number ($Re = 10^{-2}$). Without loss of generality, we set the fluid density $\rho = 1$ lbu and the relaxation time $\tau = 1$ lbu, resulting in a dynamic viscosity of the particle $\mu = 1/6$ lbu. In Figs. 2(a) and 2(d), we report simulation data for the time-evolution of the deformation index defined as

$$D(t) = \frac{r_1(t) - r_3(t)}{r_1(t) + r_3(t)}, \quad (20)$$

where r_1 and r_3 are the main particle semi-axes in the shear plane (see the top of Fig. 2 for a sketch). The simulation time is normalized with $\dot{\gamma}$. Results show a very good agreement between simulations and the time-evolution of the deformation D defined in Eq. (8), obtained from the analytical solutions of Eq. (5) (dashed lines). In addition, the steady-state value of the deformation D can be analytically estimated as a function of the triad of α as

$$D = \left[\frac{5\alpha_1(3\alpha_2 + 4\alpha_3)}{4(3\alpha_1\alpha_2 + 5\alpha_1\alpha_3 + 2\alpha_2\alpha_3 + 2\alpha_3^2)} \right] Ca, \quad (21)$$

where $Ca = \mu R \dot{\gamma} / \alpha_1$. Since Eq. (21) has been computed with $\alpha_2, \alpha_3 \neq 0$, it does not hold for a pure droplet, for which $\alpha = \bar{\alpha}(1, 0, 0)$. In the latter case, we have³⁶

$$D = \frac{19\lambda + 16}{16\lambda + 16} Ca, \quad (22)$$

with $\lambda = 1$ in the present work. Figures 2(b) and 2(e) confirm the agreement between simulation data and Eqs. (21) and (22) in the limit of small deformations (i.e., small Ca), while it diverges for larger values of D . Note that in Fig. 2(b), the theoretical prediction for cases $\alpha = \bar{\alpha}(1, 0, 1)$ and $\alpha = \bar{\alpha}(1, 1, 1)$ are so close to not being distinguishable.

In addition, to complete the picture of soft particle dynamics under shear flow, we report in Figs. 2(c) and 2(f) the inclination angle Θ (see top panel) as a function of the capillary number Ca . In the limit of small deformations and the case of a pure droplet with $\lambda = 1$, these results are again in agreement with what is expected from simulations⁶⁷ (black crosses) and the theory of Chaffey and Brenner⁶⁸ (dotted black line) which reads

$$\Theta = \frac{\pi}{4} - \frac{(19\lambda + 16)(2\lambda + 3)}{80(\lambda + 1)} Ca. \quad (23)$$

We observe a stronger dependency on Ca for non-pre-stressed particle models, probably due to the higher rigidity.

To summarize, we find a good agreement for the time-evolution of the particle deformation $D(t)$ and its steady-state value D between the analytical solution of the model [Eq. (5)] and our numerical model

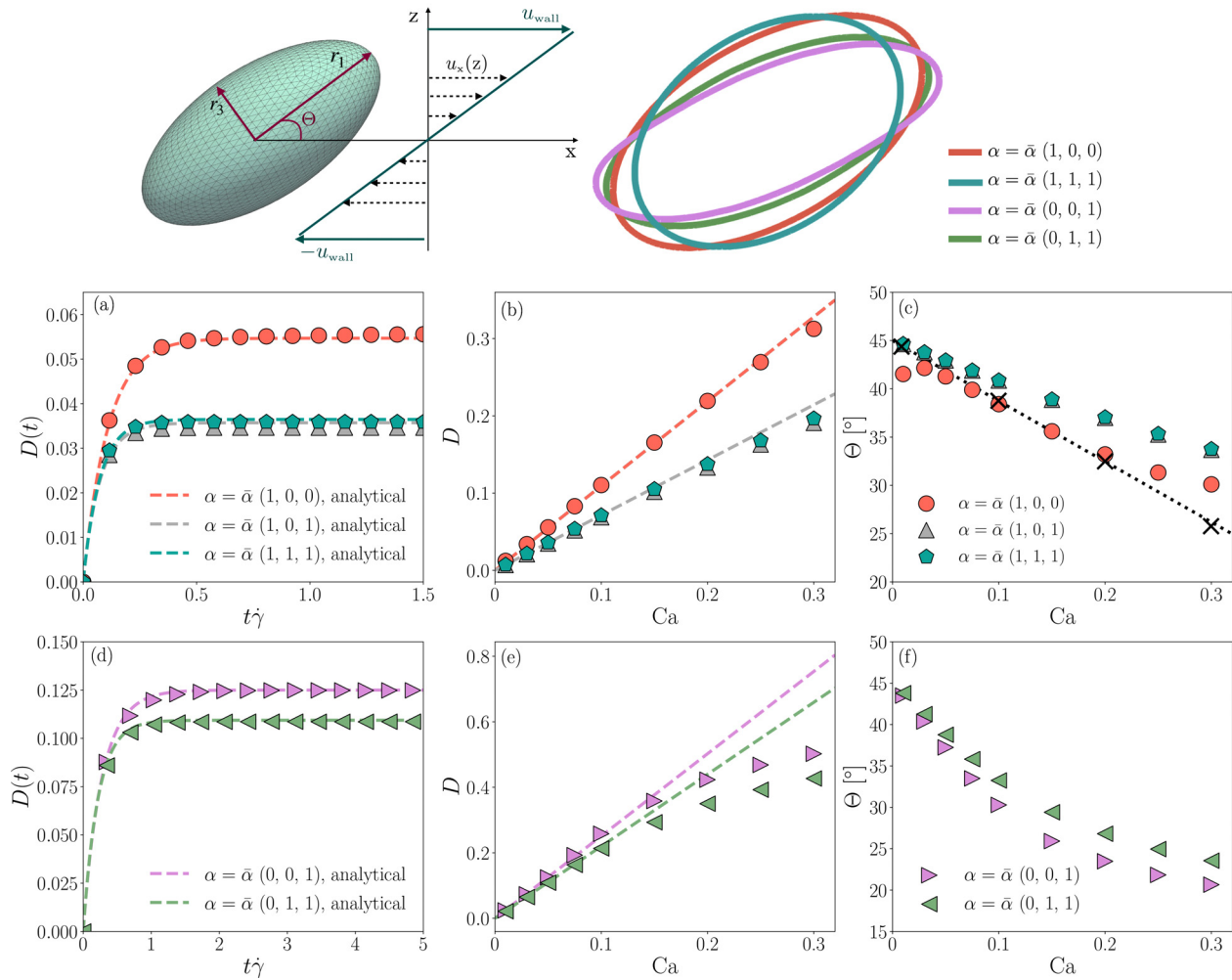


FIG. 2. Simulated experiment of a single particle under shear flow for the prestressed [panels (a–c)] and non-pre-stressed [panels (d–f)] particle models. In all panels, different symbols/colors refer to different models. Top panels: a sketch of the shear experiment and the final shape of the particle for $Ca = 0.3$. Panels (a) and (d): time evolution of the deformation index $D(t)$ [Eq. (20)] as a function of time for capillary number $Ca = 0.05$. Time is shown normalized with the shear rate $\dot{\gamma}$, and dashed lines refer to the analytical solutions of Eq. (5). Panels (b) and (e): the steady-state value of the deformation D as a function of Ca . Dashed lines draw the theoretical predictions: Eq. (22) (salmon line) for the pure droplet case and Eq. (21) (other color lines) for all the other models. Panels (c) and (f): the steady-state value of the inclination angle Θ as a function of Ca . To validate the model in the case of a pure droplet, we report black crosses from Ref. 67, and we draw dotted lines for Eq. (23).

for both coated droplets and soft particles. This is true in the limit of small deformation, which is the basic assumption behind the theory.³⁶ Furthermore, in the case of a pure droplet, both D and the inclination angle Θ follow the analytical predictions. It is worth noting that this benchmark also contributes to the validation of our generalized interface model against the interface response to an external flow.

V. WETTING DYNAMICS

A. Model validation

We now analyze the wetting dynamics of coated droplets and soft particles simulated using the interface model discussed in Sec. II. In this kind of experiment, we consider a single particle with initial

radius R and placed close to a flat wall, i.e., its initial position is such that the z -coordinate of its center-of-mass Z_{CM} is at a distance R from the wall to let it feel the action of an attractive wall–interface interaction with intensity ϵ [see Eq. (19) and Fig. 1 for a pictorial view]. In our implementation, since we do not have direct control over σ_{sb} σ_{sg} appearing in Eq. (1), we consider ϵ to play the role of an effective solid surface tension as $\epsilon \propto \sigma_{sl} - \sigma_{sg}$.

Before entering into the details of the wetting dynamics of pre-stressed and non-pre-stressed particles, we validate our implementation by quantitatively investigating the spreading dynamics of a pure droplet, $\alpha = \bar{\alpha}(1, 0, 0)$, by comparing the time evolution of the radius r of the contact area with the literature. Indeed, it has been observed that this observable scales in time as

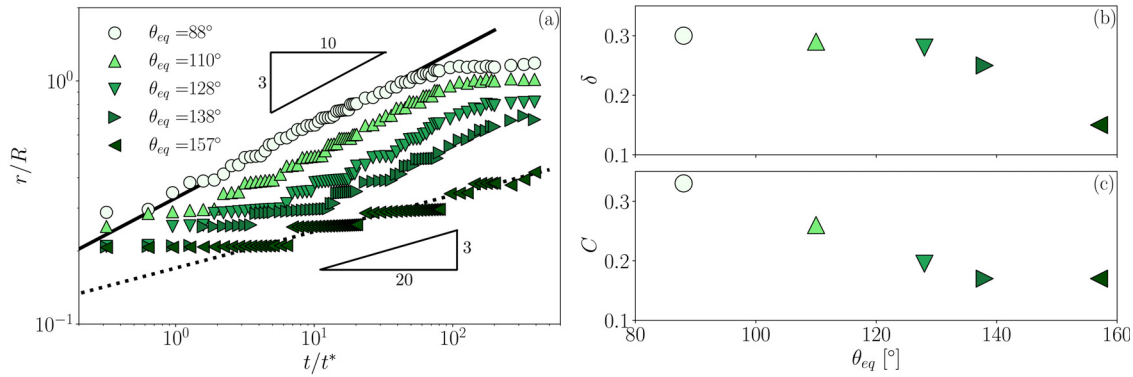


FIG. 3. Spreading experiment for a pure liquid droplet, $\alpha = (\alpha_1, 0, 0)$, on a flat surface. Panel (a): radius of the contact area r as a function of time t , where r and t are reported normalized to the initial radius R and the characteristic time $t^* = (\rho R^3 / \sigma)^{1/2}$, respectively. Different symbols/colors refer to different values of the equilibrium contact angle θ_{eq} . In all cases, we observe a scaling law $r/R = C(t/t^*)^\delta$. The solid line indicates the scaling with $\delta = 3/10$, while the dotted line refers to scaling $\delta = 3/20$. Panels (b) and (c) show the value of the dimensionless exponent δ and the dimensionless prefactor C , respectively, as a function of θ_{eq} .

$$r = Ct^\delta, \tag{24}$$

where both the prefactor C and the exponent δ can vary. When capillary forces drive the droplet spreading and inertial effects are negligible, Eq. (24) coincides with Tanner’s law,⁶⁹ predicting an exponent $\delta = 1/10$. Contrariwise, when capillary and inertial forces are balanced, it has been observed that the value of the exponent can vary with some factors, such as viscosity,⁷⁰ surface tension,⁷⁰ droplet initial shape,⁷¹ and wettability.^{70,72–74} In particular, a value of $\delta = 1/2$ has been observed in the case of very small contact angles. In Fig. 3(a), we report the time evolution of r , normalized to the initial radius R at varying equilibrium contact angles θ_{eq} . A scaling law following Eq. (24) is observed, with the exponent δ slightly decreasing at increasing θ_{eq} , in agreement with Ref. 72 [see Fig. 3(b)]. This implies that in our simulations of wetting dynamics, the inertia is not negligible and plays a role in resisting the deformation. Note that, as later highlighted in Fig. 4(a), our model can capture only cases of large contact angles ($88^\circ \leq \theta_{eq} \leq 180^\circ$); indeed δ approaches but does not reach a value of close to $1/2$, which is characteristic of small contact angles.^{70,72–74} This is comparable, for example, to the case of a liquid metal droplet, which has been observed to never assume values of $\theta_{eq} < 100^\circ$ also in the case of oxidization, suggesting that our model can be used to study such kind of system. Concerning the prefactor C [Fig. 3(c)], it decreases as θ_{eq} increases, once again in agreement with Ref. 72. Note that the “jumps” in r that are visible in Fig. 3(a) for $\theta_{eq} = 157^\circ$ originate from the numerical error in measuring very small variations of the contact area.

B. Results

With the aim of simulating the wetting dynamics of droplets with complex interface properties, we explore both prestressed ($\alpha_1 > 0$) and non-pre-stressed ($\alpha_1 = 0$) particles. For each system, characterized by $\alpha = (\alpha_1, \alpha_2, \alpha_3) = \bar{\alpha}(0/1, 0/1, 0/1)$, we apply the same strategy used for the benchmark, which we summarize again for the sake of clarity. First, we fix the value of $\bar{\alpha}$ to 10^{-4} lbu. This choice fixes both the surface tension for pre-stressed particles and the strain modulus for non-pre-stressed particles. Then, we measure θ_{eq} as a

function of the wall–particle interaction energy ϵ . In Appendix, we also discuss a resolution test for the wetting dynamics.

In Figs. 4(a) and 4(b), we report the measured θ_{eq} as a function of the ratio $\epsilon/\bar{\alpha}$ for prestressed and non-pre-stressed particle models, respectively. In Figs. 4(c) and 4(d), we report for convenience the corresponding values of $\cos \theta_{eq}$. After the largest value of $\epsilon/\bar{\alpha}$ is reported in each plot, numerical instabilities appear in the contact area region; these set the limit of applicability of our approach in terms of contact angles that can be modeled. Concerning prestressed particles, pure droplets (circles) appear to be marginally more stable with respect to the choice of ϵ than the other particles (softly coated particles, $\alpha = \bar{\alpha}(1, 0, 1)$, upward triangles; rigidly coated particles, $\alpha = \bar{\alpha}(1, 1, 1)$, pentagons) but can reach only a slightly higher contact angle ($\theta_{eq} = 88^\circ$ vs $\theta_{eq} = 79^\circ$). Notice that the cases $\alpha = \bar{\alpha}(1, 0, 1)$ and $\alpha = \bar{\alpha}(1, 1, 1)$ are very similar, meaning that when the system is very rigid, the dilatational contribution given by α_2 is not relevant for the equilibrium contact angle θ_{eq} . This result is in contrast with what we observed in the shear flow. Non-pre-stressed particle models [Figs. 4(b) and 4(d)] are stable for a more limited range of values of $\epsilon/\bar{\alpha}$. After around the value of $\epsilon/\bar{\alpha} = 1.5$, the contact angle does not drop significantly anymore. Similarly to the prestressed case, α_2 does not seem to have any influence on θ_{eq} . The behavior of $\cos \theta_{eq}$ as a function of $\epsilon/\bar{\alpha}$ follows very well the empirical behavior:

$$\cos \theta_{eq} \simeq a \tan^{-1}[b(\epsilon/\bar{\alpha} - c)] - d, \tag{25}$$

where a , b , c , and d are fitting parameters depending on the type of particle [see Table I and dashed lines in Figs. 4(c) and 4(d)]. Equation (25) differs from Eq. (1) because, as mentioned above, the model we present in this work misses the direct control of the wall surface tensions but rather drives the mechanical interaction between the particle and the solid surface. Obviously, the fitting constants represent (unknown) functions of the parameters α_1 , α_2 , α_3 , and ϵ . By increasing separately by a factor of 10 each of the components of α , as reported in Fig. 5(a), we can understand that the leading order behavior is dictated by α_1 , while α_2 and α_3 provide relatively minor changes in θ_{eq} . In addition, from Fig. 5(b), one can see that α_1 must enter in Eq. (25) in the ratio with ϵ because data for the increased α_1 (downward triangles)

24 September 2023 17:38:03

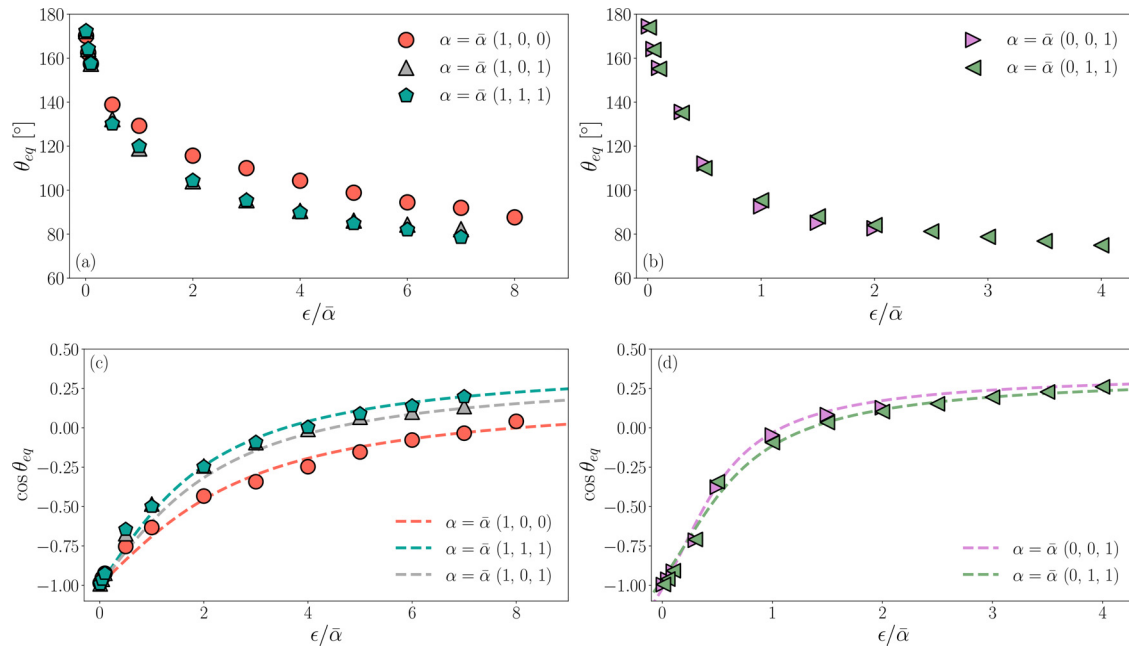


FIG. 4. Experiment of wetting dynamics. Panels (a) and (b): Equilibrium contact angle θ_{eq} as a function of the wall–particle interaction intensity ϵ , normalized to $\bar{\alpha}$. Panels (c) and (d): Corresponding values of $\cos\theta_{eq}$. Left panels [(a) and (c)] refer to prestressed particle models, while right panels [(b) and (d)] refer to non-pre-stressed particle models. In all panels, different symbols/colors refer to different models, while dashed lines indicate fitting curves with Eq. (25) (values of fitting parameters are listed in Table I). Data refer to simulations with a number of triangular faces equal to $N_f = 16820$.

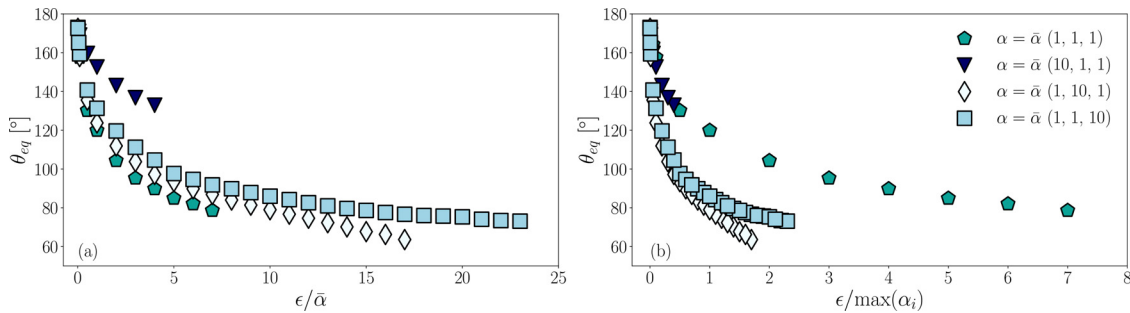


FIG. 5. Equilibrium contact angle θ_{eq} as a function of the wall–particle interaction intensity ϵ , normalized to $\bar{\alpha}$ [panel (a)] and $\max(\alpha_i)$ with $i = 1, 2, \text{ and } 3$ [panel (b)]. All data refer to the case with all components of $\alpha = (\alpha_1, \alpha_2, \alpha_3)$ turned on, but different symbols/colors refer to different “extreme” cases where one of the three parameters is increased by order of magnitude. The number of triangular faces N_f is the same as for the data in Fig. 4.

collapses onto the original case (pentagons) once plotted as a function ϵ/α_1 . The remaining parameters α_2 and α_3 , instead, do not appear to provide a similar scaling, thus meaning that these two parameters may functionally enter the other fitting parameters of Eq. (25).

VI. CONCLUSIONS

In this work, we introduced a novel numerical framework to characterize coated droplets and soft particles accurately. This approach is based on the theory of Barthès-Biesel and Rallison³⁶ and enables us to capture the unique behavior that is intermediate between that of a pure droplet and a capsule. With this generalized constitutive law, we are able to capture the special properties of a wide spectrum of

coated droplets, for example, liquid metal droplets surrounded by an oxide layer. In the present approach, the interface strain energy is written in terms of three parameters that play the role of material properties, i.e., the prestress (α_1), the resistance against area dilatation (α_2), and the resistance against shear deformation (α_3). With the choice of these three parameters, we explore different types of coated droplets, from pure liquid droplets to soft particles. We validate our methodology with the theoretical predictions and recent experiments in both shear flow and wetting experiments, and we explore the limits of the model in terms of $\alpha_{1,2,3}$. We plan to enrich this description by including new contributions to the presented model, for example, to mimic the thickness of the oxide layer in the case of liquid metal droplets.

24 September 2023 17:38:03

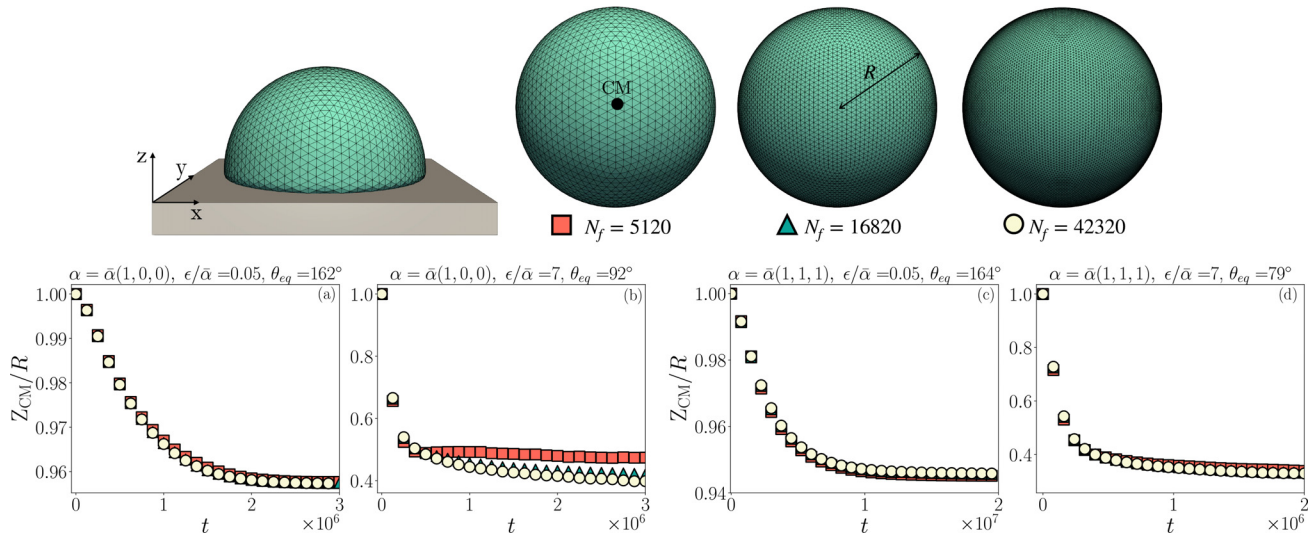


FIG. 6. Resolution test for the wetting dynamics experiment a pure droplet with $\alpha = \bar{\alpha}(1, 0, 0)$ [panels (a) and (b)] and for a mixed system with $\alpha = \bar{\alpha}(1, 1, 1)$ [panels (c) and (d)]. We compare the time evolution of the z-coordinate of the center-of-mass Z_{CM} for different resolutions, given in terms of the number of mesh triangular faces N_f . Time t is shown in lbu.

The latter could be useful to mimic the dynamics of other complex droplets such as liquid marbles.

ACKNOWLEDGMENTS

This work has received financial support from the Deutsche Forschungsgemeinschaft (DFG, German Research Foundation)—Project ID: 431791331–SFB 1452 “Catalysis at liquid interfaces” and research unit FOR2688 “Instabilities, Bifurcations, and Migration in Pulsatile Flows” (Project ID: 417989464). This work was supported by the Italian Ministry of University and Research (MUR) under the FARE Program, project “Smart-HEART.” The authors gratefully acknowledge the Gauss Center for Supercomputing e.V. (www.gauss-centre.eu) for funding this project by providing computing time through the John von Neumann Institute for Computing (NIC) on the GCS Supercomputer JUWELS⁷⁵ at Jülich Supercomputing Centre (JSC).

AUTHOR DECLARATIONS

Conflict of Interest

The authors have no conflicts to disclose.

Author Contributions

Francesca Pelusi: Conceptualization (equal); Data curation (lead); Formal analysis (lead); Investigation (lead); Methodology (equal); Software (equal); Validation (lead); Visualization (lead); Writing—original draft (lead); Writing—review and editing (lead). **Fabio Guglietta:** Conceptualization (equal); Methodology (equal); Software (equal); Validation (equal); Writing—review and editing (equal). **Marcello Sega:** Conceptualization (equal); Methodology (equal); Resources (equal); Software (equal); Supervision (equal). **Othmane Aouane:** Conceptualization (equal); Methodology (equal);

Supervision (equal). **Jens Harting:** Conceptualization (equal); Funding acquisition (lead); Project administration (lead); Supervision (lead).

DATA AVAILABILITY

The data that support the findings of this study are available from the corresponding author upon reasonable request.

APPENDIX: RESOLUTION TEST FOR WETTING DYNAMICS

Results shown in Figs. 4 and 5 required a test to choose the best resolution in terms of accuracy and computational effort. In Fig. 6, we show the time evolution of the z-coordinate of its center-of-mass Z_{CM} , normalized by the initial radius R , for a pure droplet case, $\alpha = \bar{\alpha}(1, 0, 0)$, shown in Fig. 6(a) and 6(b), and a rigidly coated droplet, $\alpha = \bar{\alpha}(1, 1, 1)$, shown in Figs. 6(c) and 6(d). We report two values of $\epsilon/\bar{\alpha}$, i.e., 0.05 [Figs. 6(a) and 6(c)] and 7 [Figs. 6(b) and 6(d)], resulting in a large and small equilibrium contact angle for both systems. As long as the contact angle is very large, then all resolutions are equivalent. However, moving toward $\theta_{eq} \sim 80^\circ$, a large number of N_f is required for more precise contact angle measurements in the case of a pure droplet. The latter statement follows from the way we compute θ_{eq} , i.e., by fitting the droplet shape with a circumference cut by a chord (i.e., the wall). To perform the fitting procedure, we take a slice of the particle mesh involving a number of nodes, which is roughly $\frac{4}{\sqrt{3}}\sqrt{\pi N_f}$. Furthermore, simulations with $N_f = 42\,320$ show the same dynamics as $N_f = 16\,820$, but they require a higher computational cost, leading to the choice made to produce the data reported in Figs. 4 and 5 to run simulations with $N_f = 16\,820$.

REFERENCES

- ¹P.-G. De Gennes, "Wetting: Statics and dynamics," *Rev. Modern Phys.* **57**, 827 (1985).
- ²F. Brochard-Wyart and P. De Gennes, "Dynamics of partial wetting," *Adv. Colloid Interface Sci.* **39**, 1–11 (1992).
- ³D. Bonn, "Wetting transitions," *Curr. Opin. Colloid Interface Sci.* **6**, 22–27 (2001).
- ⁴J. De Coninck, M. J. de Ruijter, and M. Voué, "Dynamics of wetting," *Curr. Opin. Colloid Interface Sci.* **6**, 49–53 (2001).
- ⁵T. Young, "III. An essay on the cohesion of fluids," *Philos. Trans. Roy. Soc. London* **95**, 65–87 (1805).
- ⁶B. Andreotti and J. H. Snoeijer, "Statics and dynamics of soft wetting," *Annu. Rev. Fluid Mech.* **52**, 285–308 (2020).
- ⁷J. De Coninck and T. D. Blake, "Wetting and molecular dynamics simulations of simple liquids," *Annu. Rev. Mater. Res.* **38**, 1–22 (2008).
- ⁸D. Bonn, J. Eggers, J. Indekeu, J. Meunier, and E. Rolley, "Wetting and spreading," *Rev. Modern Phys.* **81**(2), 739 (2009).
- ⁹J. H. Snoeijer and B. Andreotti, "Moving contact lines: Scales, regimes, and dynamical transitions," *Annu. Rev. Fluid Mech.* **45**, 269–292 (2013).
- ¹⁰N. Taccardi, M. Grabau, J. Debuschewitz, M. Distaso, M. Brandl, R. Hock, F. Maier, C. Papp, J. Erhard, C. Neiss *et al.*, "Gallium-rich Pd-Ga phases as supported liquid metal catalysts," *Nat. Chem.* **9**, 862–867 (2017).
- ¹¹A. Hofer, N. Taccardi, M. Moritz, C. Wichmann, S. Hübner, D. Drobek, M. Engelhardt, G. Papastavrou, E. Spiecker, C. Papp *et al.*, "Preparation of geometrically highly controlled ga particle arrays on quasi-planar nanostructured surfaces as a SCALMS model system," *RSC Adv.* **13**, 4011–4018 (2023).
- ¹²T. Daeneke, K. Khoshmanesh, N. Mahmood, I. A. De Castro, D. Esrafilzadeh, S. Barrow, M. Dickey, and K. Kalantar-Zadeh, "Liquid metals: Fundamentals and applications in chemistry," *Chem. Soc. Rev.* **47**, 4073–4111 (2018).
- ¹³F.-M. Allieux, M. B. Ghasemian, W. Xie, A. P. O'Mullane, T. Daeneke, M. D. Dickey, and K. Kalantar-Zadeh, "Applications of liquid metals in nanotechnology," *Nanoscale Horiz.* **7**, 141–167 (2022).
- ¹⁴M. Jeyakumar, M. Hamed, and S. Shankar, "Rheology of liquid metals and alloys," *J. Non-Newtonian Fluid Mech.* **166**, 831–838 (2011).
- ¹⁵K. Doudrick, S. Liu, E. M. Mutunga, K. L. Klein, V. Damle, K. K. Varanasi, and K. Rykaczewski, "Different shades of oxide: From nanoscale wetting mechanisms to contact printing of gallium-based liquid metals," *Langmuir* **30**, 6867–6877 (2014).
- ¹⁶I. D. Joshipura, K. A. Persson, V. K. Truong, J.-H. Oh, M. Kong, M. H. Vong, C. Ni, M. Alsafatwi, D. P. Parekh, H. Zhao *et al.*, "Are contact angle measurements useful for oxide-coated liquid metals?," *Langmuir* **37**, 10914–10923 (2021).
- ¹⁷L. Zheng, S. Handschuh-Wang, Z. Ye, and B. Wang, "Liquid metal droplets enabled soft robots," *Appl. Mater. Today* **27**, 101423 (2022).
- ¹⁸E. Bormashenko, "Liquid marbles: Properties and applications," *Curr. Opin. Colloid Interface Sci.* **16**, 266–271 (2011).
- ¹⁹E. Ni, T. Li, Y. Ruan, Y. Ma, Y. Wang, Y. Jiang, and H. Li, "Modeling of wetting transition of liquid metals on organic liquid surfaces," *Langmuir* **37**, 9429–9438 (2021).
- ²⁰Y. Zhao, J. Fang, H. Wang, X. Wang, and T. Lin, "Magnetic liquid marbles: Manipulation of liquid droplets using highly hydrophobic Fe₃O₄ nanoparticles," *Adv. Mater.* **22**, 707–710 (2010).
- ²¹R.-E. Avramescu, M.-V. Ghica, C. Dinu-Pirvu, D. I. Udeanu, and L. Popa, "Liquid marbles: From industrial to medical applications," *Molecules* **23**, 1120 (2018).
- ²²L. Biferale, R. Benzi, M. Sbragaglia, S. Succi, and F. Toschi, "Wetting/dewetting transition of two-phase flows in nano-corrugated channels," *J. Comput. Aided Mater. Design* **14**, 447–456 (2007).
- ²³Y. Yan and Y. Zu, "A lattice Boltzmann method for incompressible two-phase flows on partial wetting surface with large density ratio," *J. Comput. Phys.* **227**, 763–775 (2007).
- ²⁴H. Huang, D. T. Thorne, Jr., M. G. Schaap, and M. C. Sukop, "Proposed approximation for contact angles in Shan-and-Chen-type multicomponent multiphase lattice Boltzmann models," *Phys. Rev. E* **76**, 066701 (2007).
- ²⁵E. Attar and C. Körner, "Lattice Boltzmann method for dynamic wetting problems," *J. Colloid Interface Sci.* **335**, 84–93 (2009).
- ²⁶Y. Tanaka, Y. Washio, M. Yoshino, and T. Hirata, "Numerical simulation of dynamic behavior of droplet on solid surface by the two-phase lattice Boltzmann method," *Comput. Fluids* **40**, 68–78 (2011).
- ²⁷J. Hyväluoma, C. Kunert, and J. Harting, "Simulations of slip flow on nanobubble-laden surfaces," *J. Phys. Condens. Matter* **23**(18), 184106 (2011).
- ²⁸H. P. Jansen, K. Sotthewes, J. van Swigchem, H. J. Zandvliet, and E. S. Kooij, "Lattice Boltzmann modeling of directional wetting: Comparing simulations to experiments," *Phys. Rev. E* **88**, 013008 (2013).
- ²⁹L. Wang and J. Sun, "The application of axisymmetric lattice Boltzmann two-phase model on simulations of liquid film dewetting," *J. Appl. Phys.* **122**, 085305 (2017).
- ³⁰T. Akai, B. Bijeljic, and M. J. Blunt, "Wetting boundary condition for the color-gradient lattice Boltzmann method: Validation with analytical and experimental data," *Adv. Water Resources* **116**, 56–66 (2018).
- ³¹S. Zitz, A. Scagliarini, S. Maddu, A. A. Darhuber, and J. Harting, "Lattice Boltzmann method for thin-liquid-film hydrodynamics," *Phys. Rev. E* **100**, 033313 (2019).
- ³²X. Wang, B. Xu, Y. Wang, and Z. Chen, "Directional migration of single droplet on multi-wetting gradient surface by 3D lattice Boltzmann method," *Comput. Fluids* **198**, 104392 (2020).
- ³³F. Pelusi, M. Sega, and J. Harting, "Liquid film rupture beyond the thin-film equation: A multi-component lattice Boltzmann study," *Phys. Fluids* **34**, 062109 (2022).
- ³⁴X. Shan and H. Chen, "Lattice Boltzmann model for simulating flows with multiple phases and components," *Phys. Rev. E* **47**, 1815 (1993).
- ³⁵M. R. Swift, E. Orlandini, W. Osborn, and J. Yeomans, "Lattice Boltzmann simulations of liquid-gas and binary fluid systems," *Phys. Rev. E* **54**(5), 5041 (1996).
- ³⁶D. Barthès-Biesel and J. Rallison, "The time-dependent deformation of a capsule freely suspended in a linear shear flow," *J. Fluid Mech.* **113**, 251–267 (1981).
- ³⁷R. Skalak, A. Tozeren, R. Zarda, and S. Chien, "Strain energy function of red blood cell membranes," *Biophys. J.* **13**, 245–264 (1973).
- ³⁸D. Matsunaga, Y. Imai, T. Yamaguchi, and T. Ishikawa, "Rheology of a dense suspension of spherical capsules under simple shear flow," *J. Fluid Mech.* **786**, 110–127 (2016).
- ³⁹D. Barthès-Biesel and H. Sgaier, "Role of membrane viscosity in the orientation and deformation of a spherical capsule suspended in shear flow," *J. Fluid Mech.* **160**, 119–135 (1985).
- ⁴⁰R. Benzi, S. Succi, and M. Vergassola, "The lattice Boltzmann equation: Theory and applications," *Phys. Rep.* **222**, 145–197 (1992).
- ⁴¹T. Krüger, H. Kusumaatmaja, A. Kuzmin, O. Shardt, G. Silva, and E. M. Viggen, *The Lattice Boltzmann Method—Principles and Practice* (Springer, 2016).
- ⁴²Z. Guo, C. Zheng, and B. Shi, "Discrete lattice effects on the forcing term in the lattice Boltzmann method," *Phys. Rev. E* **65**, 046308 (2002).
- ⁴³C. S. Peskin, "The immersed boundary method," *Acta Numerica* **11**, 479–517 (2002).
- ⁴⁴B. Kaoui, J. Harting, and C. Misbah, "Two-dimensional vesicle dynamics under shear flow: Effect of confinement," *Phys. Rev. E* **83**, 066319 (2011).
- ⁴⁵T. Krüger, F. Varnik, and D. Raabe, "Efficient and accurate simulations of deformable particles immersed in a fluid using a combined immersed boundary lattice Boltzmann finite element method," *Comput. Math. Appl.* **61**, 3485–3505 (2011).
- ⁴⁶O. Aouane, A. Scagliarini, and J. Harting, "Structure and rheology of suspensions of spherical strain-hardening capsules," *J. Fluid Mech.* **911**, A11 (2021).
- ⁴⁷C. Bielinski, O. Aouane, J. Harting, and B. Kaoui, "Squeezing multiple soft particles into a constriction: Transition to clogging," *Phys. Rev. E* **104**, 065101 (2021).
- ⁴⁸T. Krüger, B. Kaoui, and J. Harting, "Interplay of inertia and deformability on rheological properties of a suspension of capsules," *J. Fluid Mech.* **751**, 725–745 (2014).
- ⁴⁹F. Guglietta, F. Pelusi, M. Sega, O. Aouane, and J. Harting, "Suspensions of viscoelastic capsules: Effect of membrane viscosity on transient dynamics," preprint [arXiv:2302.03546](https://arxiv.org/abs/2302.03546) (2023).
- ⁵⁰T. Krüger, D. Holmes, and P. V. Coveney, "Deformability-based red blood cell separation in deterministic lateral displacement devices—A simulation study," *Biomechanics* **8**, 054114 (2014).

- ⁵¹B. Kaoui, T. Krüger, and J. Harting, “How does confinement affect the dynamics of viscous vesicles and red blood cells?,” *Soft Matter* **8**, 9246 (2012).
- ⁵²P. Li and J. Zhang, “Similar but distinct roles of membrane and interior fluid viscosities in capsule dynamics in shear flows,” *Cardiovasc. Eng. Technol.* **12**, 232–249 (2021).
- ⁵³F. Guglietta, M. Behr, L. Biferale, G. Falcucci, and M. Sbragaglia, “Lattice Boltzmann simulations on the tumbling to tank-treading transition: Effects of membrane viscosity,” *Philos. Trans. Roy. Soc. A* **379**, 20200395 (2021).
- ⁵⁴F. Guglietta, M. Behr, G. Falcucci, and M. Sbragaglia, “Loading and relaxation dynamics of a red blood cell,” *Soft Matter* **17**, 5978–5990 (2021).
- ⁵⁵P. Li and J. Zhang, “A finite difference method with subsampling for immersed boundary simulations of the capsule dynamics with viscoelastic membranes,” *Int. J. Numer. Methods Biomed. Eng.* **35**, e3200 (2019).
- ⁵⁶F. Guglietta, M. Behr, L. Biferale, G. Falcucci, and M. Sbragaglia, “On the effects of membrane viscosity on transient red blood cell dynamics,” *Soft Matter* **16**, 6191–6205 (2020).
- ⁵⁷D. Taglienti, F. Guglietta, and M. Sbragaglia, “Reduced model for droplet dynamics in shear flows at finite capillary numbers,” *Phys. Rev. Fluids* **8**, 013603 (2023).
- ⁵⁸T. Krüger, *Computer Simulation Study of Collective Phenomena in Dense Suspensions of Red Blood Cells under Shear* (Vieweg+Teubner Verlag, 2012).
- ⁵⁹N. S. Martys and H. Chen, “Simulation of multicomponent fluids in complex three-dimensional geometries by the lattice Boltzmann method,” *Phys. Rev. E* **53**(1), 743 (1996).
- ⁶⁰J. Harting, C. Kunert, and H. J. Herrmann, “Lattice Boltzmann simulations of apparent slip in hydrophobic microchannels,” *Europhys. Lett.* **75**, 328 (2006).
- ⁶¹Q. Li, K. Luo, Q. Kang, and Q. Chen, “Contact angles in the pseudopotential lattice Boltzmann modeling of wetting,” *Phys. Rev. E* **90**(5), 053301 (2014).
- ⁶²J. Koplik and J. Banavar, “Continuum deductions from molecular hydrodynamics,” *Annu. Rev. Fluid Dyn.* **27**, 257 (1995).
- ⁶³J. Koplik and J. Banavar, “Molecular simulation of dewetting,” *Phys. Rev. Lett.* **84**, 4401 (2000).
- ⁶⁴J. Koplik, T. Lo, M. Rauscher, and S. Dietrich, “Pearling instability of nanoscale fluid flow confined to a chemical channel,” *Phys. Fluids* **18**, 032104 (2006).
- ⁶⁵D. T. Semiromi and A. Azimian, “Molecular dynamics simulation of non-droplets with the modified Lennard-Jones potential function,” *Heat Mass Transfer* **47**, 579–588 (2011).
- ⁶⁶F. Dörfler, M. Rauscher, J. Koplik, J. Harting, and S. Dietrich, “Micro- and nanoscale fluid flow on chemical channels,” *Soft Matter* **8**, 9221 (2012).
- ⁶⁷J. Gounley, G. Boedec, M. Jaeger, and M. Leonetti, “Influence of surface viscosity on droplets in shear flow,” *J. Fluid Mech.* **791**, 464–494 (2016).
- ⁶⁸C. E. Chaffey and H. Brenner, “A second-order theory for shear deformation of drops,” *J. Colloid Interface Sci.* **24**, 258–269 (1967).
- ⁶⁹L. Tanner, “The spreading of silicone oil drops on horizontal surfaces,” *J. Phys. D* **12**, 1473 (1979).
- ⁷⁰D. Legendre and M. Maglio, “Numerical simulation of spreading drops,” *Colloids Surf. A* **432**, 29–37 (2013).
- ⁷¹L. Courbin, J. C. Bird, M. Reyssat, and H. A. Stone, “Dynamics of wetting: From inertial spreading to viscous imbibition,” *J. Phys.* **21**, 464127 (2009).
- ⁷²J. C. Bird, S. Mandre, and H. A. Stone, “Short-time dynamics of partial wetting,” *Phys. Rev. Lett.* **100**, 234501 (2008).
- ⁷³A. Carlson, M. Do-Quang, and G. Amberg, “Dissipation in rapid dynamic wetting,” *J. Fluid Mech.* **682**, 213–240 (2011).
- ⁷⁴K. G. Winkels, J. H. Weijs, A. Eddi, and J. H. Snoeijer, “Initial spreading of low-viscosity drops on partially wetting surfaces,” *Phys. Rev. E* **85**, 055301 (2012).
- ⁷⁵Jülich Supercomputing Centre, “JUWELS: Modular Tier-0/1 Supercomputer at the Jülich Supercomputing Centre,” *J. Large-Scale Res. Facilities* **5**, A135 (2019).